Improved three-dimensional image correlation for surface displacement measurement

Jeffrey D. Helm
Stephen R. McNeill
Michael A. Sutton
University of South Carolina
Department of Mechanical Engineering
300 Main Street
Columbia, South Carolina 29208
E-mail: sutton@sc.edu

Abstract. A PC-based, 3-D surface profile and displacement measurement system capable of micron-level accuracy using moderately priced off-the-shelf equipment has been developed. For use in field applications, a simplified calibration process using precision grids and camera translations is developed. An improved image correlation process is developed which corrects for perspective distortions due to viewpoint differences between the two cameras. The accuracy of the system was assessed experimentally and results expressed using several different error measures, including a new error measure proposed by the authors. The accuracy for both the profile and displacement measurement systems was established through a series of profile and translation tests. The baseline tests confirmed that the measurement system is capable of highly accurate full-field measurements. The system was also used successfully to measure both the bending of a clamped circular plate under pressure loading and the local buckling which occurs during tension loading of a cracked plate.

Subject terms: computer vision; stereo vision; digital image correlation with perspective effects; three-dimensional displacement measurement.

Paper 23045 received Apr. 22, 1995; revised manuscript received Dec. 4, 1995; accepted for publication Dec. 4, 1995. This paper is a revision of a paper presented at the SPIE conference on Videometrics III, November 1994, Boston, Massachusetts. The paper presented there appears (unrefereed) in SPIE Proceedings Vol. 2350.

1 Introduction

Two-dimensional digital image correlation has been used successfully for many years to measure the in-plane displacement field in a variety of planar problems.[1–3] In addition to requiring planar surfaces, the technique is further restricted to (a) predominantly in-plane deformations and (b) cases where the recording camera can be set perpendicular to the object surface.

Improving the measurement of object positions in three dimensions presents several challenges, including (a) development of a simple, yet effective calibration method for both cameras, (b) determination of several camera parameters through optimization and (c) improving the accuracy in locating points in space using the calibrated camera parameters. Relative to (a) and (b), which are required to establish the spatial orientation and operating characteristics for each camera, much work has been done. Tsai[4,5] has divided the optimization process into two parts: determination of the 3-D orientation and (x,y) position; and determination of the effective focal length, distortion coefficient and z position. Weng, Cohen and Herniou's[6] two-step calibration system uses a set of linear equations to fit some of the camera parameters and then improves all of the parameters using nonlinear optimization. The measurement system of Luo, Chao and Sutton[7,8] uses a laborious, time-consuming process for camera calibration involving multiple precision translations of an object and a fully nonlinear optimization process to obtain the camera parameters.

Relative to (c), the extension of digital image correlation into three dimensions for use in experimental mechanics is recent.[7–9] Luo et al. used an image correlation algorithm which (a) matches *square* subsets in one image to *square* subsets in another and (b) uses the data to triangulate and estimate the 3-D displacement field. The lack of perspective correction in the matching process limits the range of camera orientations which can be used for accurate image evaluation. Furthermore, due to the complexity of the calibration process used in their work and the lack of an interface for rapidly and effectively acquiring images, the overall stereo system is best suited for use in laboratory experiments. Recent work by Helm et al.[10] has demonstrated that an accurate and simple method for camera calibration can be developed.

In this paper, a three-dimensional surface displacement measurement system is described. The proposed method (a) includes perspective effects, which has improved the accuracy and extended the range of usefulness for the system, (b) includes a custom-designed software interface so that the overall system is flexible, easy to set up and easy to operate, and (c) is applicable to a variety of problems having different size scales. Furthermore, by defining a new measure for the accuracy of the system, the *resolution based error* (RBE), the accuracy of the proposed system is shown to compare favorably with previous work. Finally,

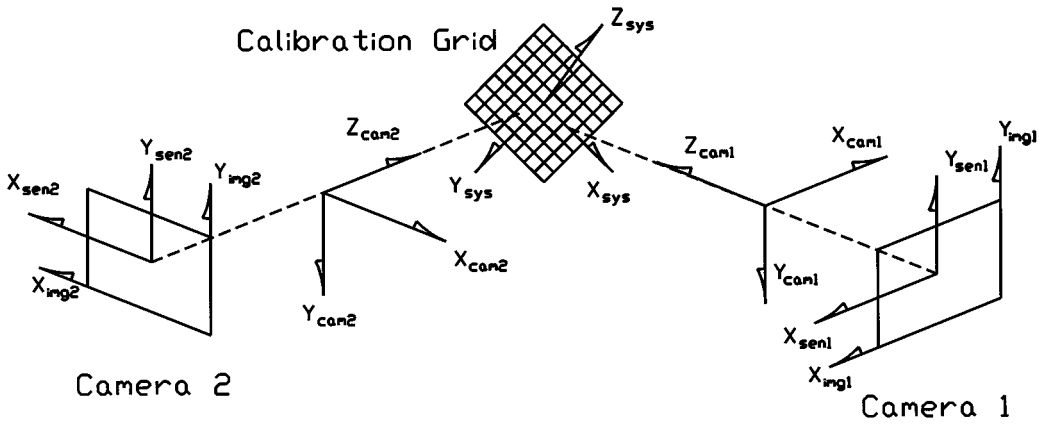

Fig. 1 Various coordinate systems used in stereo vision modeling.

data obtained from structural experiments clearly show that the system is both accurate and versatile.

2 System Model

The theoretical development for stereo imaging is well documented. In this work, a brief summary of the key equations and assumptions are presented. First, the camera and lens system are modeled as a pinhole device. To increase the accuracy of such models, they are modified to correct for Seidel lens distortion.[11] The imaging characteristics of a camera modeled in this manner can be described by five parameters: the pinhole distance (phd), the location of the center of the image (C_x, C_y), a lens distortion factor κ and the aspect ratio λ for the sensors. The aspect ratio λ is the ratio of the size of a pixel in the Y direction to the size in the X direction. The location of points in space and on the images will be described using seven coordinate systems, as illustrated in Figure 1. Note that the system-wide coordinate system $(X_{\text{sys}}, Y_{\text{sys}}, Z_{\text{sys}})$ serves as a bridge between the two cameras; the position of the system-wide coordinate system and its orientation are established during the calibration process. The location of each of the cameras will be developed relative to this coordinate system.

Coordinates $(X_{\text{cam1}}, Y_{\text{cam1}}, Z_{\text{cam1}})$ and $(X_{\text{cam2}}, Y_{\text{cam2}}, Z_{\text{cam2}})$ describe locations in space relative to the camera coordinate system for camera 1 (CAM1 system) and camera 2 (CAM2 system), respectively, as shown in Figure 1, with the origin of each camera system located at each camera's pinhole. The four remaining coordinate systems are used to translate the data from pixel coordinates in each camera into physical dimensions in the CAM1 and CAM2 systems.

The relationship between the camera coordinates and the system coordinates can be written in the following form. Aligning the camera and system coordinate systems and then consecutively rotating the camera system by (a) α about Z_{sys}, (b) γ about the rotated Y_{sys} and (c) β about the twice rotated X_{sys} yields the following rotational transformation that will convert system coordinates into camera coordinates:

$$[R] = \begin{bmatrix} \cos\alpha\cos\gamma & -\sin\alpha\cos\gamma & \sin\gamma \\ \sin\alpha\cos\beta+\cos\alpha\sin\gamma\sin\beta & \cos\alpha\cos\beta-\sin\alpha\sin\gamma\sin\beta & -\cos\gamma\sin\beta \\ \sin\alpha\sin\beta-\cos\alpha\sin\gamma\cos\beta & \cos\alpha\sin\beta+\sin\alpha\sin\gamma\cos\beta & \cos\gamma\cos\beta \end{bmatrix}. \tag{1}$$

If the origin of the system coordinates is then translated with respect to the rotated camera coordinates by the amounts X_0, Y_0, Z_0, then we have

$$[T] = \begin{bmatrix} X_0 \\ Y_0 \\ Z_0 \end{bmatrix}, \tag{2}$$

and the total transformation from system to camera coordinates can be written

$$\begin{bmatrix} X_{\text{cam}} \\ Y_{\text{cam}} \\ Z_{\text{cam}} \end{bmatrix} = [R] \begin{bmatrix} X_{\text{sys}} \\ Y_{\text{sys}} \\ Z_{\text{sys}} \end{bmatrix} + [T]. \tag{3}$$

Using similar triangle relationships, the projection from camera coordinates to sensor coordinates is

$$\frac{X_{\text{cam}}}{X_{\text{sen}}} = \frac{Y_{\text{cam}}}{Y_{\text{sen}}} = \frac{Z_{\text{cam}}}{\text{phd}}. \tag{4}$$

This results in the following projection equations:

$$X_{\text{sen}} = \frac{\text{phd}\ X_{\text{cam}}}{Z_{\text{cam}}}, \quad Y_{\text{sen}} = \frac{\text{phd}\ Y_{\text{cam}}}{Z_{\text{cam}}}. \tag{5}$$

Using Eq. (4), it is apparent that projection of a known sensor coordinate results in a one-to-many transformation. Therefore, the two-dimensional to three-dimensional projection from the sensor plane to a 3-D position dictates the use of two cameras if a unique position is to be determined. To allow for lens distortion, a correction term can be written:

$$\overline{X_{\text{sen}}} = \frac{X_{\text{sen}}}{1+\kappa(X_{\text{sen}}^2+Y_{\text{sen}}^2)^{1/2}}, \quad \overline{Y_{\text{sen}}} = \frac{Y_{\text{sen}}}{1+\kappa(X_{\text{sen}}^2+Y_{\text{sen}}^2)^{1/2}}, \tag{6}$$

and the inverse of (6),

$$X_{\text{sen}}=\frac{2\overline{X_{\text{sen}}}}{1+[1-4\kappa(\overline{X_{\text{sen}}^2}+\overline{Y_{\text{sen}}^2})]^{1/2}},$$
$$Y_{\text{sen}}=\frac{2\overline{Y_{\text{sen}}}}{1+[1-4\kappa(\overline{X_{\text{sen}}^2}+\overline{Y_{\text{sen}}^2})]^{1/2}}, \tag{7}$$

can be applied at the sensor plane.

To access the image data stored in the computer, the sensor coordinates must be related to image coordinates. This is accomplished with a simple transformation of the sensor coordinates. This transformation requires the location of the image center (C_x, C_y) and the value for the aspect ratio λ of the camera/digitizer system. The transformation from the sensor plane to the image coordinates is written

$$X_{\text{img}}=\overline{X_{\text{sen}}}+C_x, \quad Y_{\text{img}}=\lambda\overline{Y_{\text{sen}}}+C_y. \tag{8}$$

Equations (1) to (8), which are well known in computer vision, relate coordinates for an object point $(X_{\text{sys}}, Y_{\text{sys}}, Z_{\text{sys}})$ to its position in the image. These equations form the basis for the camera calibration procedure used in this work.

3 Camera Calibration

3.1 *General*

Equations (1) to (8) are used to relate 2-D positions in the camera sensor plane to 3-D positions in space. The stereo vision method in this work uses two cameras to determine 3-D positions of a point by using the 2-D images of the same point from both cameras. Since Eqs. (1) to (8) relate 3-D points to 2-D images for each camera, accurate 3-D measurement requires that Eqs. (1) to (8) must accurately model the imaging process. Calibration refers to the determination of the eleven parameters α, β, γ, X_0, Y_0, Z_0, C_x, C_y, phd, κ and λ in Eqs. (1) to (8) for each camera used in the stereo vision system so that accurate, 3-D surface measurements can be obtained. The parameters α, β, γ, X_0, Y_0, Z_0 describe the overall orientation and position of a camera and are *extrinsic* parameters. The *intrinsic* parameters C_x, C_y, phd, κ and λ describe the internal traits of the camera.

3.2 *Calibration Procedure*

3.2.1 *Overview*

First, since the aspect ratio is solely a function of the computer–digitizing-board interface, the value for λ is determined independently. It is emphasized that the experiments required for determination of λ need be performed only once; thereafter, the value is unaltered by changes in lens configuration, camera arrangement, magnification factor or other parameters. Furthermore, since the camera–digitizing-board combination is the same for both cameras, the value obtained for λ can be used for both cameras. Each camera is calibrated separately to obtain the remaining ten parameters using a precision grid common to both cameras. It is noted that, since both cameras are calibrated using simultaneously recorded images of the same grid (i.e., both cameras have the same system coordinate system), the positions of the cameras relative to each other are known after the calibration. Thirdly, to complete the calibration for each camera, each camera is translated perpendicular to the sensor plane by a known distance. It is noted that several translations can be used in the calibration process, but only one translation is required.

3.2.2 *Determination of* λ

A series of images is acquired with the grid positioned perpendicular to the optical axis of a camera and with the calibration grid lines oriented at approximately 45 deg to the sensor grid of that camera. The intersection points in the image of the grid are found using the following procedure: the image is converted to binary form through thresholding; the section of the grid to be used is selected; the computer searches for black pixels along each line in the selected area to obtain data points locating the grid lines; the data are weighted by the difference between the original gray level and the threshold level; the data points for each line are fitted with a nonoblique parabola using nonlinear least squares; the intersections of these curves are calculated; the intersection points are divided into several 5×5 square subset groupings within the 9×9 grid; the average of the ratios $\Delta Y_{\text{img}}/\Delta X_{\text{img}}$ of alternate diagonal subset vertices from twenty grid images is used as the initial estimate for λ. Since the value for the aspect ratio λ is solely determined by a combination of the physical layout of the sensor grid, the timing circuits in the cameras and the digitizing board, this process is only required to be performed one time. For the camera/digitizer combination used in this work, the value was determined to be $\lambda\approx0.962$; additional translation experiments performed by the authors[9] improved the estimate to $\lambda=0.9617$. This value is used for both cameras in the tests described in the following sections to determine the accuracy of the system.

3.2.3 *Camera calibration*

A typical stereo vision setup for camera calibration is shown in Fig. 2. The calibration grid, which would be located near the specimen position shown in Fig. 2, establishes the position and orientation of the system coordinate system, with the initial plane of the grid defined to have $Z_{\text{sys}}=0$. The camera system is positioned so that images of the grid can be acquired. The grid is oriented at approximately 45 deg to the row direction in each camera with the images of the grid roughly centered in the field of view for each camera; lighting on the grid is adjusted to produce roughly even illumination of the background with the grid lines clearly visible; and each camera is focused on the grid using a large f number to maximize the depth of field.

The camera calibration process is based on a series of images of the calibration grid. Acquisition of the calibration images proceeds as follows: (a) images are acquired simultaneously by both cameras in the initial position; (b) both cameras are translated perpendicular to the sensor plane by ΔZ_1 and a new set of images of the grid acquired;

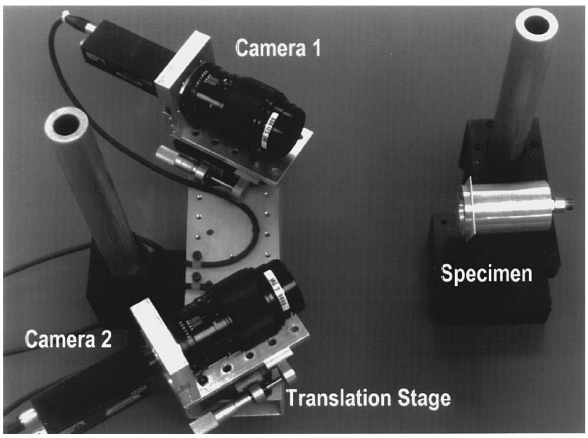

Fig. 2 Typical experimental stereo vision arrangement.

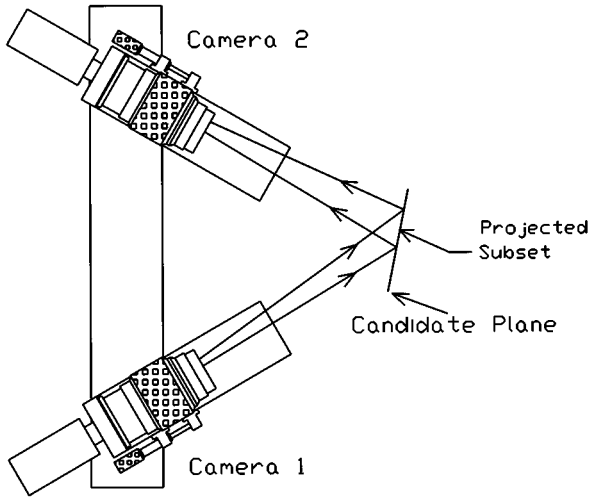

Fig. 3 Schematic of perspective projection for profile analysis.

(c) part (b) is repeated for several ΔZ_J so that independent checks on the accuracy of the calibration process can be performed.

Once the images are acquired, the intersection points for the grid are obtained using the procedure described in the previous section. The intersection points provide a series of known positions $(X_{\text{sys}}, Y_{\text{sys}}, 0)_J$. These points form the foundation for the calibration process. To determine the sensor position for all of the known grid positions, Eqs. (1) to (4) can be written

$$Y_{\text{sen}} = \text{phd}\frac{\begin{bmatrix}(\sin\alpha\cos\beta+\cos\alpha\sin\gamma\sin\beta)X_{\text{sys}} \\ +(\cos\alpha\cos\beta-\sin\alpha\sin\gamma\sin\beta)Y_{\text{sys}}+Y_0\end{bmatrix}}{\begin{bmatrix}(\sin\alpha\sin\beta-\cos\alpha\sin\gamma\cos\beta)X_{\text{sys}} \\ +(\cos\alpha\sin\beta+\sin\alpha\sin\gamma\cos\beta)Y_{\text{sys}} \\ +Z_0+\Delta Z_{\text{cam}}\end{bmatrix}}, \tag{9}$$

$$X_{\text{sen}} = \text{phd}\,\frac{(\cos\alpha\cos\gamma\,X_{\text{sys}}-\sin\alpha\cos\gamma\,Y_{\text{sys}}+X_0)}{\begin{bmatrix}(\sin\alpha\sin\beta-\cos\alpha\sin\gamma\cos\beta)X_{\text{sys}} \\ +(\cos\alpha\sin\beta+\sin\alpha\sin\gamma\cos\beta)Y_{\text{sys}}+Z_0 \\ +\Delta Z_{\text{cam}}\end{bmatrix}}. \tag{10}$$

The $(X_{\text{sen}}, Y_{\text{sen}})_J$ positions are corrected for lens distortion and converted to image coordinates using Eqs. (5) to (8). The locations of the intersections in the image $(X_{\text{int}}, Y_{\text{int}})_J$ are acquired. This allows a direct comparison of projected intersection points with the imaged positions for each point. The error function is written

$$\text{Error} = \sum_{J=1}^{n}\{[x_{\text{img }J}-x_{\text{int }J}]^2+[y_{\text{img }J}-y_{\text{int}-J}]^2\}. \tag{11}$$

Equation (11) is minimized for each camera in the stereo system using a Levenberg-Marquardt nonlinear optimization method[12] to establish the ten parameters.

4 Full-Field Profiling and Three-Dimensional Displacement Measurement

Once calibration is completed, the stereo vision system can be used for either profiling or full, three-dimensional displacement measurements. Profiling can be performed with either a projected random pattern or a random pattern bonded to the surface.

4.1 *Profiling*

As shown schematically in Figure 3, the profiling analysis can be applied to any pair of images taken by camera 1 and camera 2 at the same time. Assuming that an object is composed of a large number of small planar surfaces, the image taken by camera 1 is projected onto a candidate plane; the candidate plane is the flat plane which best approximates the surface location of the object at the projected position. The candidate plane is described in CAM1 coordinates by two direction angles θ, ϕ and the variable Z_p representing the location of the intersection of the plane and the optic axis for camera 1. The following equation describes the candidate plane:

$$\begin{aligned}&X_{\text{cam1}}\cos\theta+Y_{\text{cam1}}\cos\phi+Z_{\text{cam1}}\cos[(1-\cos^2\phi \\ &\quad-\cos^2\theta)^{1/2}] \\ &\quad=Z_p\cos[(1-\cos^2\phi\cos^2\theta)^{1/2}],\end{aligned} \tag{12}$$

where

$(\xi,\phi,\theta)=$ angles orienting the normal to a candidate plane,

$$\xi=(1-\cos^2\phi-\cos^2\theta)^{1/2},$$

$Z_p=$ location on candidate plane of the point $(0,0,Z_p)$ where the optic axis intersects.

The process for profiling is as follows. First, a subset of intensity values from the image in camera 1 is chosen. For

each pixel in camera 1's subset, the image coordinates $(X_{\text{img }2}, Y_{\text{img }2})$ are converted to sensor coordinates and corrected for lens distortion using Eqs. (6), (8). Secondly, given $(X_{\text{sen }1}, Y_{\text{sen }1}, \text{phd}_1)$, the coordinates $(Y_{\text{cam }1}, Z_{\text{cam }1})$ in the CAM1 system can be obtained using Eq. (4) and the inverse of Eq. (5) to give

$$Y_{\text{cam }1} = X_{\text{cam }1}\,\frac{Y_{\text{sen }1}}{X_{\text{sen }1}}, \quad Z_{\text{cam }1} = \frac{X_{\text{cam }1}\,\text{phd}_1}{X_{\text{sen }1}}. \tag{13}$$

Thirdly, using Eq. (13) in Eq. (12), an expression for $X_{\text{cam }1}$ can be obtained in terms of known parameters $X_{\text{sen }1}$, $Y_{\text{sen }2}$, phd_1 and the candidate plane's parameters, θ, ϕ and Z_p. Using this expression in Eqs. (13), similar expressions for $Y_{\text{cam }1}$ and $Z_{\text{cam }1}$ are obtained. The expressions are written

$$X_{\text{cam }1} = \frac{[X_{\text{sen }1} Z_p \cos(1-\cos^2\phi\cos^2\theta)^{1/2}]}{[\text{phd}_1 \cos(1-\cos^2\phi-\cos^2\theta)^{1/2} + Y_{\text{sen }1}\cos\phi, + X_{\text{sen }1}\cos\theta]},$$

$$Y_{\text{cam }1} = \frac{[Y_{\text{sen }1} Z_p \cos(1-\cos^2\phi-\cos^2\theta)^{1/2}]}{[\text{phd}_1 \cos(1-\cos^2\phi\cos^2\theta)^{1/2} + Y_{\text{sen }1}\cos\phi, + X_{\text{sen }1}\cos\theta]}, \tag{14}$$

$$Z_{\text{cam }1} = \frac{[\text{phd}_1 Z_p \cos(1-\cos^2\phi-\cos^2\theta)^{1/2}]}{[\text{phd}_1 \cos(1-\cos^2\phi-\cos^2\theta)^{1/2} + Y_{\text{sen }1}\cos\phi, + X_{\text{sen }1}\cos\theta]}.$$

Equation (14) gives the 3-D projected position (in the CAM1 system) of the pixel with position $(X_{\text{sen }1}, Y_{\text{sen }1})$. Fourthly, the position $(X_{\text{cam }1}, Y_{\text{cam }1}, Z_{\text{cam }1})$ is converted into image coordinates in the CAM2 system, $(X_{\text{img }2}, Y_{\text{img }2})$, using Eqs. (1) to (8) and the known relationship between the CAM1 and CAM2 coordinate systems. This process, known as back-projection, includes correction for camera 2 lens distortion. It is worth noting that the process of back-projecting the points to the camera 2 sensor plane from the candidate plane requires only the position $(X_{\text{cam }1}, Y_{\text{cam }1}, Z_{\text{cam }1})$ and parameters determined by calibration of the two cameras. Finally, the optimal position of the candidate plane is obtained by varying Z_p, θ and ϕ and minimizing the difference in gray levels between the camera 1 and camera 2 subsets. The required initial estimates for the candidate plane's parameters are obtained by the user through a PC-based Windows graphical interface written for this purpose. A subpixel interpolation scheme[13] is used to improve the accuracy of the estimated gray levels in Camera 2, and a cross-correlation error function[14] is employed for the optimization process to reduce the effects of lighting variations between the cameras. To obtain full-field data, subsequent initial estimates for neighboring subsets are derived from the results for the previous subset.

4.2 *Three-Dimensional Displacement Measurement*

As shown in Figure 4, for displacement measurements the candidate plane is allowed to undergo translations and rotations. Therefore, the points established by the projection

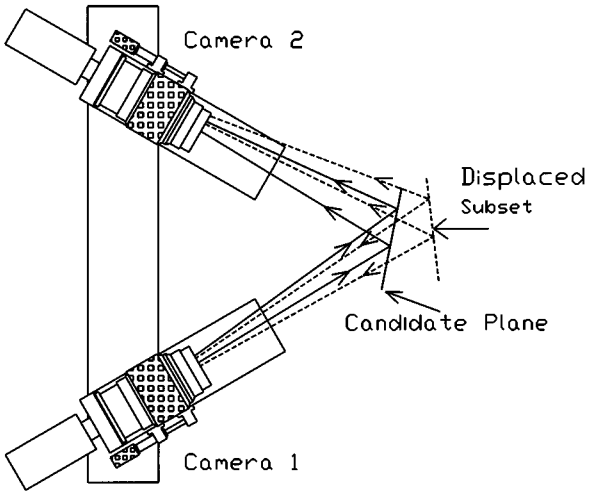

Fig. 4 Schematic of perspective projection for displacement measurement analysis.

of any subset from camera 1 onto the candidate plane will also translate and rotate with the candidate plane. These displaced points are then projected back into camera 1 and camera 2. The gray levels for the projections are compared with the recorded gray levels from images taken by cameras 1 and 2 after loading the specimen. A cross-correlation error function similar to the one for profiling is used to determine the initial location of the surface point, as well as translations of the point and rotations of the surface at the point.

In this case, the error function is based on the difference between the gray levels that are projected from camera 1's initial image and (a) the initial image from camera 2, (b) the recorded gray levels from camera 1 at some later time t_2, and (c) the gray levels from camera 2 at time t_2. The differences in the gray levels from all three images are optimized simultaneously to establish the best-fit candidate plane and its displacements.

It is noted that this process includes perspective distortion *directly* through the pinhole camera model used for projection. This is a substantial improvement over previous approaches[7] which directly matched square subsets in the images and used strict center-of-the-subset triangulation to locate 3-D positions. Finally, since information about the orientation of the surface as well as its position and displacement in space is obtained, the system can handle relatively large in-plane and out-of-plane rotations.

5 Experiments

5.1 *Experimental Setup*

The equipment required to obtain images includes two cameras mounted on translation stages, a computer with a video digitizing board, a target grid, a light source and the various specimens. The cameras chosen for the calibration were SONY XC-77 CCD cameras with an effective resolution of 512×480 pixels. The lenses for the cameras were Canon 100 mm F4 macro lenses. A custom camera mount was developed (see Fig. 2) that served (a) as an adapter from the Canon FD mount of the lens to the camera's C

mount threads, (b) as the main support for the lens and the camera and (c) as the connection point to the translation stage. This provided a very stable camera configuration that aided in the alignment of the camera and the translation stage. Translation of the camera required for the calibration was carried out with a Newport translation stage with a least count accuracy of 0.001 mm.

The cameras were connected to a Data Translation DT 2859 multiplex board, which was in turn connected to a Data Translation DT2862 digitizing board. A 33 MHz 486DX computer was used to acquire data and run the analysis. A separate video monitor was used to view the live images from the cameras. Lighting for the experiments was provided by an adjustable incandescent lamp connected to two fiber optic bundles.

A calibration grid was used to determine the aspect ratio and the other ten parameters for each camera. The grid used in this work is a contact measuring reticule with a 10×10 mm grid divided equally into 100 squares. The line thickness of the grid was 0.03 mm, and the grid had a point-to-point accuracy of ±4 μm. To improve contrast, the grid was mounted on a translucent plate that was backlit.

For calibration, the two cameras were mounted in the same horizontal plane, with the total angle between cameras ≈60 deg; the distance to the calibration grid was approximately 400 mm.

5.2 *Calibration Experiments*

Using the setup described in the previous section, a series of out-of-plane translations for each camera were performed; the cameras were moved 0, ±1, ±2, ±3, ±4, and ±5 mm and images were acquired. Baseline experiments confirmed that only two positions are needed, $\Delta Z_{\text{cam}}=0$ and ΔZ, to determine all parameters accurately. In this work, the calibrated parameters are determined using the 0 mm and 5 mm calibration images. An independent measure for the accuracy of the calibration was determined using data from 2 mm and 4 mm calibration images.

Relative to determining the ''error'' in the calibrated system, it is noted that several measures for error have been proposed. For example, Tsai[4,5] proposed the radius of ambiguity zone (RAZ) defined by

$$\text{RAZ}=\frac{\Sigma_{i=1}^{n}[(\Psi_i-\psi_i)^2+(Y_i-\varphi_i)^2]^{1/2}}{n}, \tag{15}$$

where

Ψ,Y = system coordinates of the actual intersections of the grid,

ψ,φ = projected positions of the test data on the object plane

n = number of points.

Weng[6] defined a normalized stereo calibration error (NSCE) as

$$\text{NSCE}=\frac{1}{n}\sum_{i=1}^{n}\left[\frac{(\Psi_i-\psi_i)^2+(Y_i-\varphi_i)^2}{\epsilon_i^2(f_u^{-2}+f_v^{-2})/12}\right]^{1/2}, \tag{16}$$

where

Ψ,Y = camera coordinates of the actual x,y intersections of the grid,

ψ,φ,ϵ = projected positions of the test data in camera coordinates,

f_u,f_v = pinhole distances for the horizontal and vertical directions,

n = number of points.

The NSCE error analysis does have the advantage that it factors out the influence of the test setup. However, the NSCE appears to be based on the assumption that one cannot measure the position of a point in the image with accuracy better than one pixel.

In this work, we define a new error measure, resolution based error (RBE). The RBE is written

$$\text{RBE}=\frac{1}{n}\sum_{i=1}^{n}[(X_{\text{img }i}-X_{\text{int }i})^2+(Y_{\text{img }i}-Y_{\text{int }i})^2]^{1/2}, \tag{17}$$

where

$X_{\text{int}},Y_{\text{int}}$ = projected locations of the actual grid intersections on the image,

$X_{\text{img}},Y_{\text{img}}$ = data point locations in an image.

The advantages of the RBE are that (a) it indicates how well the camera model and data generator work together to fit the grid data, (b) it is independent of the system's magnification factor, and (c) it can be used to establish an approximate value for the RAZ for other camera systems having different resolutions and/or magnification factors.

Using the 2 mm and 4 mm calibration images, the value for RBE is estimated to be 0.08 pixels for the current system. A comparison of the various error measures for previous stereo systems to the values for the current work indicates that (a) the RBE for the current system is at least five times smaller than the RBE values for previous setups and (b) Luo's high RBE and small RAZ indicates that the relatively high accuracy is mainly due to a high magnification factor.

5.3 *Profile Experiment*

In this work, a ground steel plate with a random speckle pattern was used. Prior to imaging, the average surface roughness for the plate was obtained using a Taylor-Hobson Surtronic 3P profilometer; the average roughness from the profile measurement was 1.775 μm. The plate was then placed in the field of view of both cameras and two images were acquired. The set of images were analyzed using the profiling analysis procedure described previously. The initial estimates for the location of the candidate plane were established by visually matching three image points in camera 1 to the same points in camera 2. A total of 566 points were analyzed over a 400×310 rectangular image area. The profile for the ground steel surface is shown in Figure 5.

For comparison with the profilometer, the test data were fitted with a best fit plane to establish a median zero level of profile; the average magnitude of variation in the surface

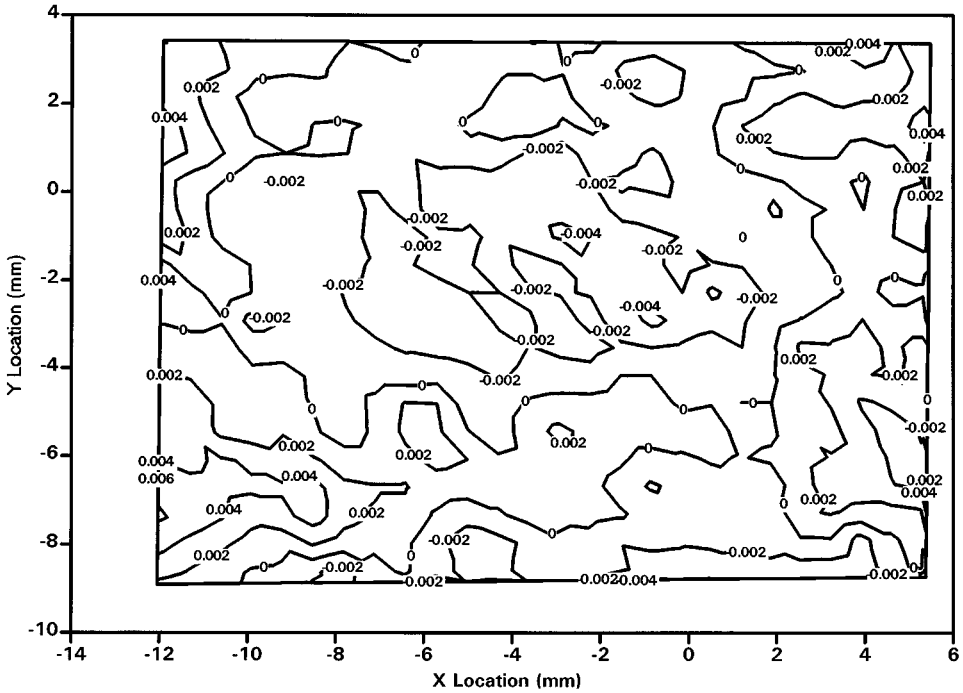

Fig. 5 Surface profile for ground steel plate.

heights relative to the best fit plane for 566 points was 1.745 μm, which compared well with the profilometer measurement.

5.4 *Pressure Loading of Clamped Circular Plate*

A random speckle pattern was applied to a flat circular aluminum plate with thickness t of 0.762 mm. The modulus of elasticity E for the plate was determined experimentally to be 71.0 GPa, and Poisson's ratio ν was 0.334. The plate was clamped to a pressure fixture using eight equally spaced bolts as shown in Figure 6. A calibration of the camera system was performed using the previously described procedure, and the fixture was mounted with the aluminum plate visible in both cameras. An initial set of images was taken to establish the baseline for the displacement of the plate. The fixture was then connected to a source of compressed air. The pressure behind the plate was increased in 68.9 kPa steps until a pressure of 689 kPa was obtained. At each step, a pair of images was taken for analysis. For each pressure the displacement relative to the initial plate position was analyzed at 121 locations over a 341 by 341 pixel area.

The experimental out-of-plane displacement data along several radial lines were compared with the theoretical out-of-plane displacement[15] described by the following equations:

$$y = y_c - \frac{M_c r^2}{2D(1+\nu)} + LT_y,$$

$$D = \frac{Et^3}{12(1-\nu^2)}, \quad y_c = \frac{qa^4}{64D}, \quad M_c = \frac{qa^2(1+\nu)}{16}, \quad LT_y = \frac{qr^4}{64D}, \tag{18}$$

where q is the pressure, a is the radius of the plate and r is the distance from the center of the plate to any point. It is noted that, for comparison with the experimental data, the value for the plate radius was not known precisely, due to slippage of the plate during loading; the plate diameter used, $d = 13.385$ mm, was obtained through least-square fitting of the experimental displacement data for various radial lines at all of the measured pressures to the theoretical formula predictions. The data and theoretical curves are plotted in Figure 7. The data clearly follow the trends calculated from the theory.

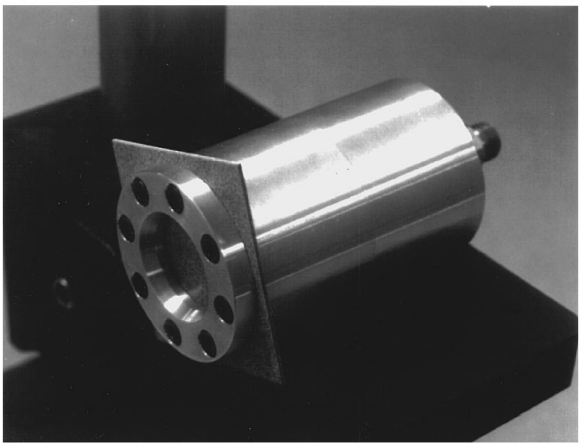

Fig. 6 Clamped circular plate fixture for pressurization experiments.

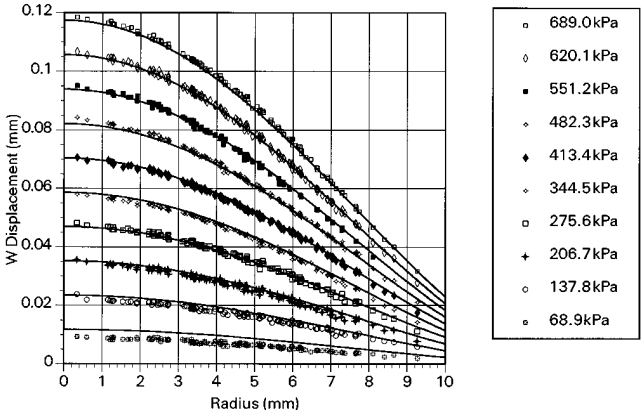

Fig. 7 Comparison of experimental data and theoretical predictions for several radial lines in circular plate.

5.5 *Tension Loading of a Center-Cracked Panel*

To verify that the stereo measurement system can be used for large specimens in a more challenging laboratory environment, tension tests were performed at NASA Langley Research Center in the Mechanics of Materials Laboratory. The actual specimen, which was machined from 2024-T3 aluminum, is shown in Figure 8. The specimen's dimensions are shown in Figure 9. The center crack was generated by (a) using a jeweler's saw to notch the center region and (b) fatigue precracking the specimen using the procedure outlined in previous work.[16] After notching the specimen, and prior to fatigue precracking, one side of the specimen was lightly spray painted white with acrylic enamel and a dusting of black enamel was used to obtain a random pattern.

Prior to performing the experiments, the stereo system was located approximately 83.8 cm from the specimen so that a 20 cm×20 cm region on the specimen could be imaged throughout the test. A series of calibration tests were performed; the tests indicated that the dimensional accuracy for the setup was ±0.050 mm. After completing the calibration tests, the calibration grid was removed and the specimen installed in the loading fixture. All tests were performed in displacement control using a 100 kip hydraulic Instron test system.

During the tests, a 20 cm by 20 cm region (see Figure 9) was imaged throughout the loading. Images were acquired until the onset of crack growth; this occurred when the loading exceeded 11 kips. The out-of-plane displacement field was evaluated at several load levels. Results for loadings of 1, 8, 10 and 11 kips are shown in Figure 10.

Results from the tests indicated that (a) during the initial loading phase, the specimen straightened, (b) as the tension loading increased beyond 5 kips, local buckling began to occur just above and below the crack line, and (c) large scale buckling of the crack region was observed just prior to crack growth.

6 Conclusions

An improved 3-D measurement system has been developed which (a) is fully PC-based, (b) includes a user-friendly Windows interface to simplify the calibration and data ac-

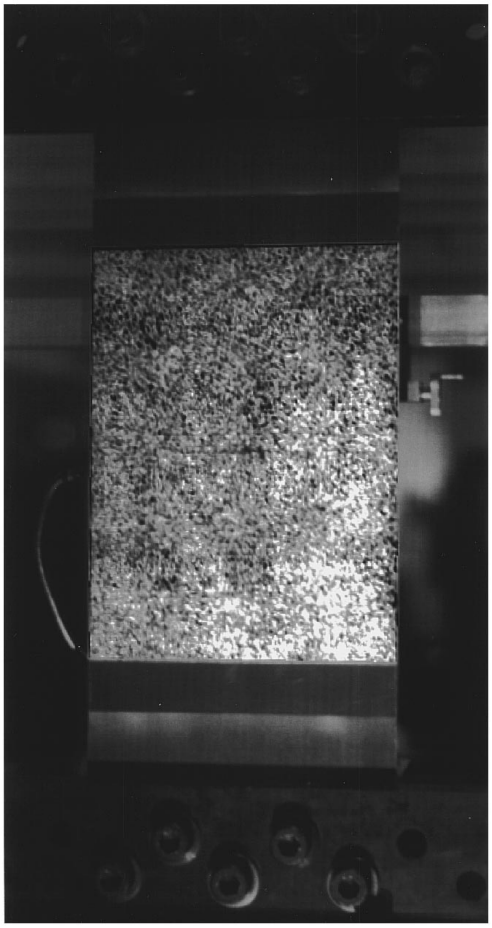

Fig. 8 Photograph of center-cracked specimen in loading grips.

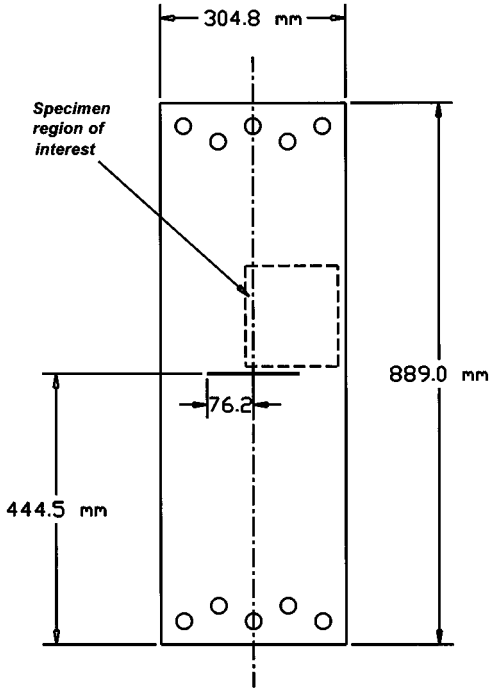

Fig. 9 Dimensions for center-cracked specimen.

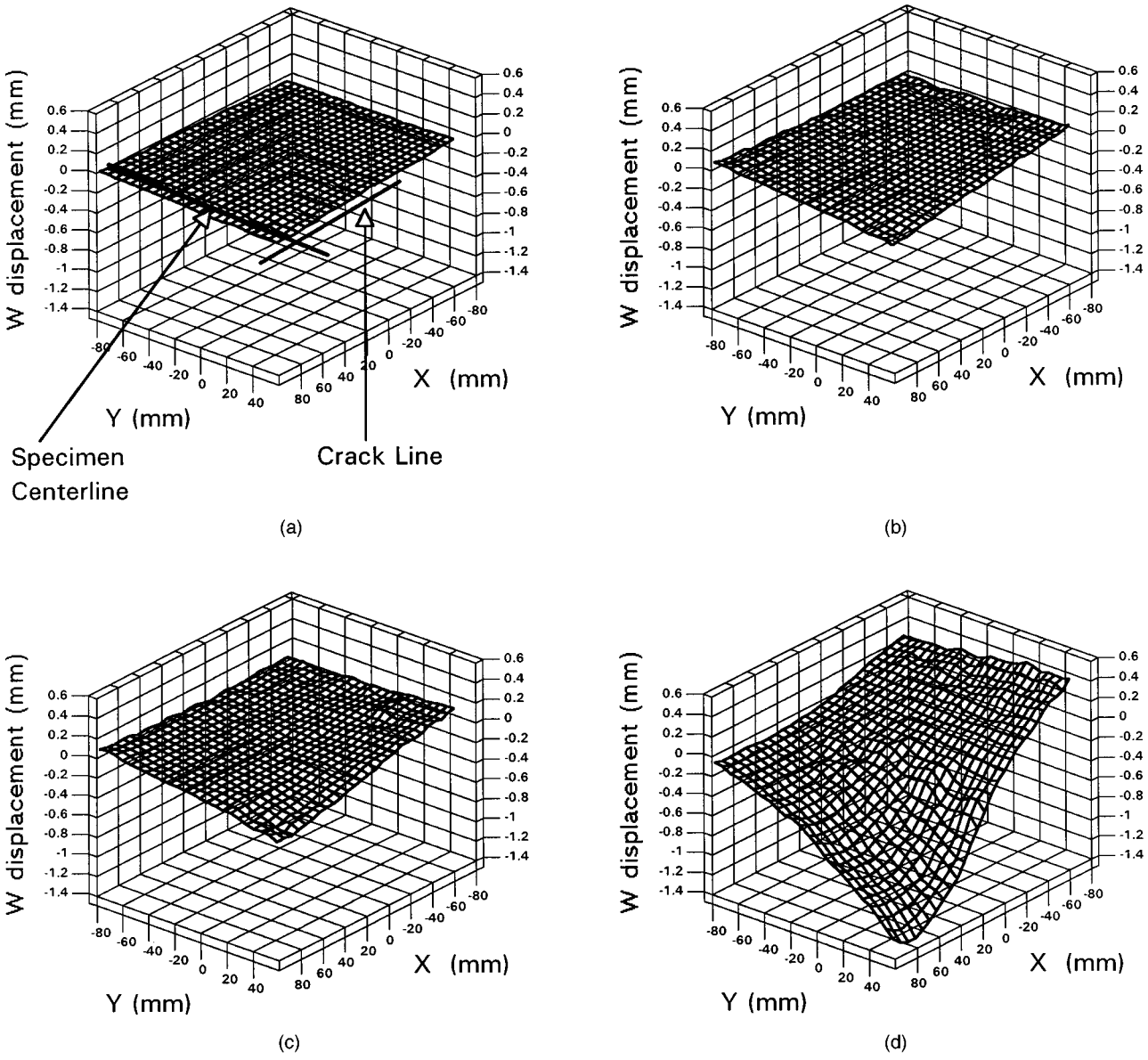

Fig. 10 Out-of-plane displacement field for region of interest in tests of wide, center-cracked panels. Loading is: (a) 4.45 kN; (b) 35.60 kN; (c) 44.5 kN; and (d) 48.95 kN.

quisition process, (c) introduces simple, efficient and accurate methods for calibration and (d) includes perspective effects in the three-dimensional displacement measurement process to increase the accuracy and range of usefulness for the method.

To demonstrate the accuracy of the method, a new measure of error is defined by the authors, the resolution based error (RBE); the calibration system in this work has RBE $=0.086$, which is much smaller than values for other stereo vision systems reported in the literature.

Several experiments have been performed to demonstrate (1) the versatility of the system, (2) the accuracy of the measurements and (3) the ability of the system to be used in challenging laboratory environments without degrading the quality of the measurements.

Acknowledgments

The authors wish to thank Dr. Charles E. Harris and Dr. James C. Newman, NASA Langley Research Center, Mechanics of Materials Branch, and Dr. David Dawicke, AS&M Services, for their encouragement and technical advice. Furthermore, the financial support for this work through NASA grant NAG-1-1489 is deeply appreciated. In addition, the encouragement provided by Dr. Walter Jones and the financial support of AFOSR through grant F49620-94-1-0448 are gratefully acknowledged.

References

1. S. R. McNeill, W. H. Peters, and M. A. Sutton, ''A study of fracture parameters by digital image processing,'' *Proc. 18th Midwestern Mechanics Congress*, pp. 267–271 (1983).

2. S. R. McNeill, W. H. Peters, and M. A. Sutton, ''Estimation of stress intensity factor by digital image correlation,'' *Eng. Fracture Mech.* **28**(1), 101–112 (1987).
3. D. S. Dawicke and M. A. Sutton, ''Crack-tip-opening angle measurements and crack tunneling under stable tearing in thin sheet 2024-T3 aluminum alloy,'' NASA Contractor Report 191523, Sep. 1993.
4. R. Y. Tsai, ''An efficient and accurate camera calibration technique for 3D machine vision,'' in *Proc. IEEE International Conf. on Computer Vision and Pattern Recognition*, pp. 364–374 (1986).
5. R. Y. Tsai, ''A versatile camera calibration technique for high accuracy 3D machine vision metrology using off-the-shelf TV cameras and lenses,'' *IEEE J. Robotics and Automation* **RA-3**(4), 324–344 (1987).
6. J. Weng, P. Cohen, and M. Herniou, ''Camera calibration with distortion models and accuracy evaluation,'' *IEEE Trans. Pattern Anal. and Mach. Intell.* **14**(10), 965–980 (1992).
7. P. F. Luo, Y. J. Chao, and M. A. Sutton, ''Application of stereo vision to 3-D deformation analyses in fracture experiments,'' *Opt. Eng.* **33**(3), 981–990 (1994).
8. P. F. Luo, Y. J. Chao, M. A. Sutton, and W. H. Peters III, Accurate measurement of three-dimensional deformations in deformable and rigid bodies using computer vision, *Exp. Mech.* **30**(2), 123–132 (1993).
9. Z. L. Kahn-Jetter and T. C. Chu, ''3-D displacement measurements using digital image correlation and photogrammetry techniques,'' *Exp. Mech.* **30**(1), 10–16 (1990).
10. J. D. Helm, M. A. Sutton, and S. R. McNeill, '' 3-D digital image correlation for surface displacement measurements,'' in *SPIE Videometrics III, Proc. SPIE* **2350**, 32–45 (1995).
11. M. Born and E. Wolf, *Principles of Optics*, 3rd ed., pp. 203–233, Pergamon Press (1964).
12. W. H. Press, S. A. Teukolsky, W. T. Vetterling, and B. P. Flannery, *Numerical Recipes in C*, 2nd ed., pp. 683–688, Cambridge University Press (1992).
13. M. A. Sutton, S. R. McNeill, J. Jang, and M. Babai, ''Effects of subpixel image restoration on digital correlation error estimates,'' *Opt. Engr.* **27**(10), 870–877 (1988).
14. H. A. Bruck, S. R. McNeill, M. A. Sutton, and W. H. Peters, ''Digital image correlation using Newton-Raphson method of partial differential corrections,'' *Exp. Mech.* **29**(3), 261–267 (1989).
15. S. P. Timoshenko and J. N. Goodier, *Theory of Elasticity*, 3rd ed., McGraw-Hill (1970).
16. D. S. Dawicke and M. A. Sutton, ''CTOA and crack tunneling measurements in thin sheet 2024-T3 aluminum alloy,'' *Exp. Mech.* **34**(4), 357–369 (1994).

Jeffrey D. Helm is a graduate student at the University of South Carolina. He received his master's degree from the University in 1995 and his bachelor's in 1992. He is currently involved in research with NASA's aging aircraft program. His current interest includes 3-D digital image correlation and its application to several areas of research, including medicine and fracture mechanics.

Stephen R. McNeill obtained his undergraduate degree in mechanical engineering from the Georgia Institute of Technology in 1978. He received his master's degree in mechanical engineering from Auburn University in 1982 and his PhD degree in mechanical engineering from the University of South Carolina in 1986. Dr. McNeill joined the mechanical engineering faculty at the University of South Carolina in 1986. Dr. McNeill has written 20 journal papers in the area of computer vision in experimental mechanics and manufacturing. His current areas of interest are 2-D and 3-D digital image correlation for determining surface deformation and surface profiling. Current applications include fracture mechanics, reverse engineering, and nondestructive testing.

Michael A. Sutton received his BS and MS from Southern Illinois University in 1972 and 1974. He received his PhD from the University of Illinois in 1981. Dr. Sutton joined the faculty in the Department of Mechanical Engineering at the University of South Carolina in 1982 and is now a professor in the department. In 1985, Dr. Sutton was selected by the National Science Foundation as a Presidential Young Investigator for his work in computer vision and solid mechanics. In 1992, he was selected by the Society of Experimental Mechanics to receive the B. J. Lazan Award for his pioneering experimental work in computer vision and solid mechanics. Dr. Sutton has published nearly 70 journal articles and has coauthored two book chapters, one for the *Experimental Mechanics Handbook* and one for the *Handbook for Experimental Methods in Fracture Mechanics*. His current areas of research are experimental and analytical fracture mechanics, 2-D and 3-D computer vision, numerical methods and mathematical modeling of problems.